

Self-Sustained Penrose Excitation of Accretion Disks: A Spin-Regulated Mechanism for Super-Eddington Quasar Luminosities

JUN WAKABAYASHI¹

¹*Independent Researcher, Japan*

ABSTRACT

We present a high-spin, near-threshold equatorial radiative channel that (i) sustains super-Eddington luminosities and (ii) naturally enforces a sub-unity spin ceiling, explaining why spins do not exceed unity in practice. Compactness-limited transparency (ℓ) gates the observable power, and a simple torque balance links the luminosity to the same control that sets the ceiling. The framework is immediately testable via three co-occurring hooks at high spin and high accretion rate: (1) a 20–120 keV high-energy shoulder favored over a featureless continuum by ΔAICc or $\Delta\text{BIC} \geq 6$; (2) lag hardening from X to UV/optical; and (3) equator-aligned X-ray polarization with a rising degree. The path to falsification is explicit: in vetted high-spin, high- λ quasars, failure to recover at least two hooks—after excluding heavy absorption, extreme inclination, and high-compactness cases—would refute the scenario.

Keywords: Quasars — Accretion, accretion disks — Black hole physics — Relativistic processes

EXECUTIVE SUMMARY

1. Near-extremal spins enable a compactness-gated *equatorial* radiative channel that sustains $L/L_{\text{Edd}} > 1$ while self-limiting the spin.
2. The lever is repeated Penrose-like coupling at the ISCO-ergoregion interface, depositing power back into the disk and extracting angular momentum.
3. The framework predicts three joint hooks: a hard X/MeV shoulder (20–120 keV, obs), lag hardening (X→UV/optical), and equator-aligned X-ray polarization.
4. Screens remove confounders: Compton-thick absorption, extreme inclination, and high compactness ($\ell < 30$ required).
5. **Kill-shot:** in vetted high-spin/high- λ quasars, failure to recover ≥ 2 hooks (after screens) refutes the framework.

1. INTRODUCTION

In brief — Observed super-Eddington luminosities and sub-unity spin ceilings motivate an *equatorial*, spin-regulated channel beyond viscous accretion alone.

Threshold, transparency, and a natural spin ceiling. Near-threshold activation at high spin, gated by compactness-limited transparency ($\ell \lesssim 30$), se-

lects an equatorial radiative channel that both sustains $L/L_{\text{Edd}} > 1$ and imposes a spin ceiling. This section sketches the mechanism and sets up testable consequences with explicit falsification (Eqs. (2)–(11); Fig. 1).

Recent reviews have noted persistent tensions between thin-disk expectations and observations—e.g., systematically large continuum-emitting sizes from microlensing and reverberation, and wavelength-dependent lags exceeding simple reprocessing models (e.g., E. M. Cackett & A. Zoghbi 2021; M. Sun et al. 2020). These tensions motivate considering *additional inner-disk heating* beyond local viscous dissipation. Near $a_* \rightarrow 1$, an *equatorial, magnetically assisted Penrose-like split* provides a *testable route* to such reheating (Sec. 2.3), with observational hooks and falsification criteria (Sec. 3.1). The possibility of extracting rotational energy from the ergoregion was first pointed out by R. Penrose (1969); R. Penrose (2002).

Scope and modeling stance.—We present a phenomenological framework: the microphysics of beam formation, transport, and equatorial deposition is intentionally kept agnostic, while the *observable consequences* of such coupling are made explicit and falsifiable. This stance allows clean confrontation with data now and provides a clear interface to future GRMHD/plasma studies that could instantiate the coupling agent.

Boundary conditions are not fixed near $a_ \rightarrow 1$.*—Much of the literature treats the inner disk, magnetosphere,

and ergoregion with effectively fixed cross-component boundary conditions. We instead emphasize that near-extremal spin the boundaries themselves evolve: frame dragging enlarges and reshapes the ergoregion, the ISCO approaches it, and the equatorial return path becomes thin and resistive. In this coupled regime an equatorial current sheet is generically required by the global field topology; shear and flux loading drive plasmoid-dominated reconnection; and the resulting split redistributes (E, L) so that a negative-energy branch is absorbed by the hole while a gain branch vents as a narrow equatorial quasi-beam, part of which returns to heat the inner disk.

2. THEORETICAL FRAMEWORK

In brief — Near-threshold Kerr coupling at the ISCO–ergoregion interface supplies disk heating while extracting spin, under a compactness gate $\ell < 30$.

All elements invoked below act outside the event horizon; the coupling operates in the ergoregion and deposits energy in the equatorial flow, avoiding assumptions about interior or singularity-scale physics. *Abbreviations and references.* We use *FFE* for the force-free, magnetically dominated limit ($\rho_e \mathbf{E} + \mathbf{J} \times \mathbf{B} \approx 0$, $\mathbf{J} \cdot \mathbf{E} = 0$) and *GRMHD* for ideal magnetohydrodynamics evolved on a Kerr background (S. S. Komissarov 2004; S. E. Gralla & T. Jacobson 2014; W. E. East & H. Yang 2018; Z. Pan 2018). We use *PIC* for first-principles kinetic simulations that resolve reconnection and plasmoid formation in the ergospheric current sheet (K. Parfrey et al. 2019; A. Bransgrove et al. 2021). Throughout we group references as (FFE/GRMHD) versus (PIC).

2.1. Kerr Energy Reservoir

In brief — A near-extremal Kerr hole stores $\sim 0.29 Mc^2$ of rotational energy that can power luminous episodes.

For a Kerr black hole of mass M and spin a_* , the extractable rotational energy is

$$E_{\text{rot}}(a_*) = \left[1 - \sqrt{\frac{1}{2} \left(1 + \sqrt{1 - a_*^2} \right)} \right] Mc^2, \quad (1)$$

reaching $\sim 0.29 Mc^2$ as $a_* \rightarrow 1$.

2.2. Spin-Triggered Coupling

In brief — A steep activation above $a_{\text{th}} \simeq 0.97$ sets both the luminosity lever and a self-imposed spin ceiling.

We posit a threshold spin a_{th} above which an ergoregion-coupled agent activates. The effective coupling follows

$$\epsilon_{\text{coup}}(a_*) = \begin{cases} 0, & a_* \leq a_{\text{th}}, \\ \epsilon_{\text{max}} \left(\frac{a_* - a_{\text{th}}}{1 - a_{\text{th}}} \right)^n, & a_* > a_{\text{th}}, \end{cases} \quad (2)$$

where ϵ_{max} is the saturation cap and n controls activation sharpness. *Activation threshold.* The equatorial coupling turns on steeply once the spin exceeds a threshold a_{th} . In our fiducial calibration, the rise is rapid near $a_* \simeq 0.97$, setting the lever for both luminosity boost and spin regulation (cf. Eqs. (2)–(11)).

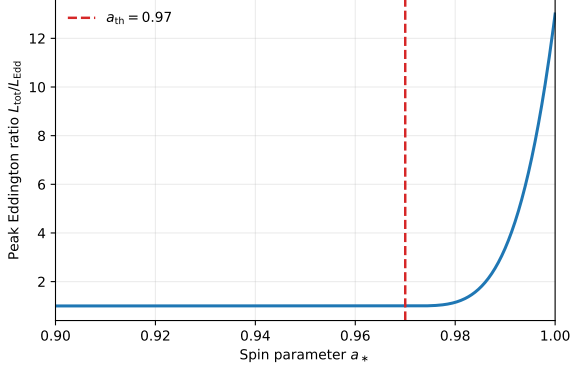


Figure 1. Activation turns on steeply above the threshold. Peak $L_{\text{tot}}/L_{\text{Edd}}$ rises rapidly once $a_* > a_{\text{th}}$, setting the lever for luminosity and spin regulation (cf. Eqs. (2)–(11)).

Unless noted, we adopt the following fiducials for figures and estimates: $M = 10^9 M_\odot$, $\eta_{\text{acc}} = 0.1$, $\epsilon_{\text{max}} = 0.1$, $n = 2$, $R_0 = 10^2$, and $\alpha = 50$; the illustrative threshold is $a_{\text{th}} \simeq 0.97$. *Micro-bridge.* While we keep microphysics agnostic, the fiducial range $\epsilon_{\text{coup}} \sim 10^{-2}$ – 10^{-1} is broadly consistent with energy-release fractions seen in near-horizon, plasmoid-dominated reconnection in recent GRMHD studies. For the present framework we only assume that ϵ_{coup} rises sharply above a_{th} and saturates below ϵ_{max} ; detailed calibration is left for future simulations.

Phenomenological parameters and physical ranges.—The cap ϵ_{max} limits equatorial deposition efficiency by energy-budget and pair-compactness constraints; n controls activation sharpness above a_{th} as an effective criticality index of the coupling geometry. (R_0, α) regulate the dissipation footprint to maintain transparency, trading compactness against reprocessing. We restrict these to physically plausible ranges and view them as interfaces for future GRMHD/plasma calibration, not curve-fitting knobs.

Sensitivity and saturation.—The activation $\epsilon_{\text{coup}}(a_*)$ is intentionally steep: (a_{th}, n) set the narrowness of the “spin ceiling”. In practice ϵ_{coup} and the leakage fraction depend nonlinearly on flux loading and \dot{M} , with possible saturation arbitrarily close to the extremal limit. We therefore treat $(a_{\text{th}}, n, \epsilon_{\text{max}}, \alpha)$ as calibration parameters to be fixed by future GRMHD-in-ergoregion testbeds.

Power partition.—We allow the extracted rotational power to partition between a polar BZ jet and an equatorial feedback channel:

$$P_{\text{ext}} = P_{\text{jet}} + P_{\text{eq}}, \quad f_{\text{BZ}} + f_{\text{eq}} = 1.$$

Near $a_* \rightarrow 1$, f_{eq} can become substantial (radio-quiet, radiation-dominated states), while f_{BZ} dominates in

radio-loud systems; hybrid states are possible in transient MAD-like regimes.

2.3. Mechanism sketch: a leaky equatorial return path

In brief — Equatorial reconnection ejecta split in the ergoregion; a negative-energy branch is absorbed while a quasi-beam returns to heat the inner disk.

Projectile sufficiency.—Reconnection ejecta (plasmoids) in the ergoregion carry specific energy E and angular momentum L . A Penrose split requires a branch with $E - \Omega_H L < 0$ (horizon condition).² Tension-driven redistribution during ejection changes L by $\Delta L \sim \mathcal{O}(r_g v_\phi)$ and reconnection outflows can reach $v \sim 0.1$ – $0.5c$ in high- S sheets; hence tens-of-percent shifts in L suffice to place a fraction on the negative-energy branch, with the complement forming the *positive-energy branch* (equatorial quasi-beam). Near-extremal spin brings the ISCO into close contact with the ergoregion and enforces an equatorial return current sheet at their interface. Shear and flux loading thin the sheet until it becomes tearing-unstable; reconnection then ejects plasmoids as a chain of narrow, equator-following pulses. These ejecta provide the “projectile” required by a Penrose-like energy split: within the ergoregion, a fraction of the flow is placed on negative-energy-at-horizon trajectories while the counterpart gains energy and escapes. The extraction condition is simply

$$E - \Omega_H L < 0. \quad (3)$$

cf. R. Penrose 1969; R. Penrose 2002. so the black hole’s rotational energy pays for the escaping branch. The centrifugal barrier and toroidal tension form an equatorial nozzle, so a growing fraction of the circuit power vents as a collimated equatorial quasi-beam while the DC return still closes globally. A modest back-flow coupling ($\epsilon_{\text{coup}} \sim 10^{-2}$ – 10^{-1}) suffices to heat the inner disk and regenerate magnetic flux, closing a self-sustained loop. The active zone and leakage fraction increase monotonically with spin (and also depend nonlinearly on flux loading and accretion rate), with possible saturation arbitrarily close to the extremal limit.

² Notation follows Fig. 2.

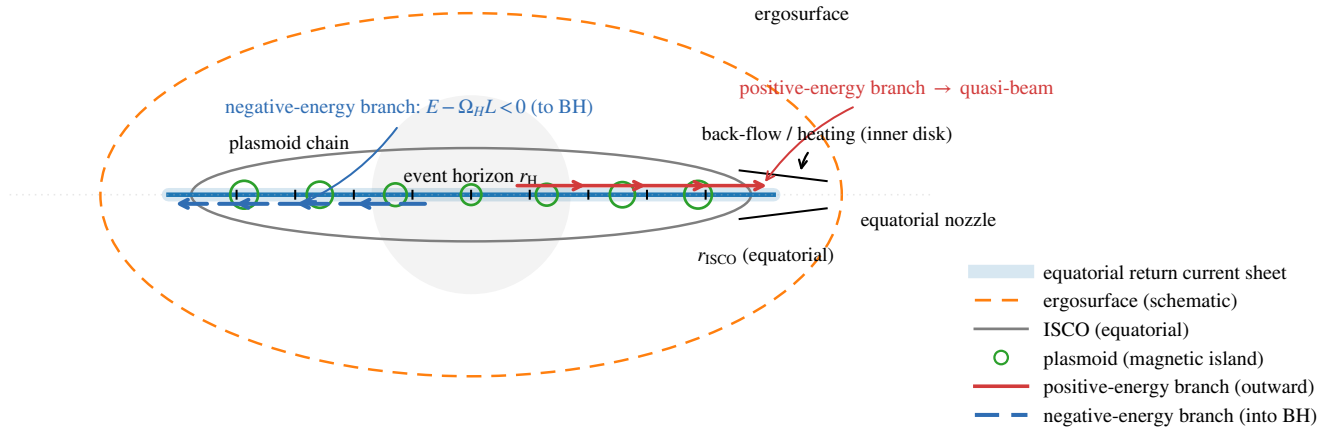


Figure 2. Equatorial Penrose trigger: negative vs. positive branches.

Plasma from the inner disk/plunging region enters the ergosphere and splits kinematically: a *negative-energy branch* with $E - \Omega_H L < 0$ falls through the *event horizon* (r_H), while a *positive-energy branch* emerges as an equatorial quasi-beam that reheats the inner rim near r_{ISCO} (R. Penrose 1969; R. Penrose 2002). Landmarks—ergosurface, r_{ISCO} , and the equatorial return current sheet (blue ribbon)—are indicated; branches are shown as *red solid* (positive) and *blue dashed* (negative) to match Eq. (3).

(FFE/GRMHD: S. S. Komissarov 2004; W. E. East & H. Yang 2018; Z. Pan 2018; PIC: K. Parfrey et al. 2019; A. Bransgrove et al. 2021).

Why an equatorial, quasi-collimated branch?—Near $a_* \rightarrow 1$ the combination of (i) the equatorial centrifugal barrier, (ii) strong toroidal fields generated by shear (hoop stress), and (iii) pressure deficits carved by intermittent reconnection outflows forms an “equatorial nozzle”. The *positive-energy branch* therefore propagates as a narrow, radiation-supported quasi-beam rather than escaping along the poles. Because the transport remains largely collisionless/Poynting-dominated until it reprocesses in the inner disk, and because the dissipation footprint is extended ($R_{\text{eff}} \sim 10^2\text{--}10^3 r_g$), the pair compactness along the beam stays low, consistent with the transparency requirement of Eq. (6).

2.4. Self-Sustained Penrose Excitation

In brief — A modest feedback fraction $\epsilon_{\text{coup}} \sim 10^{-2} - 10^{-1}$ closes the loop, sustaining bright states without pair-choking.

The mean extraction power is $\langle P_{\text{ext}} \rangle = E_{\text{rot}}/\tau$, and with duty cycle d the instantaneous power during active phases is $P_{\text{ext}} \sim \langle P_{\text{ext}} \rangle/d$. Here τ denotes the effective extraction e-folding timescale of the rotational-energy reservoir, i.e., $\langle P_{\text{ext}} \rangle = E_{\text{rot}}/\tau$ using Eq. (1).

2.5. Disk Dissipation and Scale

In brief — An extended footprint $R_{\text{eff}} \sim 10^2 - 10^3 r_g$ keeps ℓ low so the hard component remains transparent.

A fraction $\epsilon_{\text{coup}}(a_*)$ of P_{ext} is deposited into the disk:

$$L_{\text{self}} = \epsilon_{\text{coup}} P_{\text{ext}}, \quad (4)$$

and the dissipation spreads over an effective radius

Self-transparency (physical note).—The scaling $R_{\text{eff}} \approx R_0[1 + \alpha(\epsilon_{\text{coup}}/\epsilon_{\text{max}})]r_g$ phenomenologically captures geometric spreading, multi-zone deposition, and increased scattering mean free paths as the equatorial quasi-beam heats and rarefies the inner disk corona. Our results require $R_{\text{eff}} \sim 10^2\text{--}10^3 r_g$ during bright episodes to keep the pair compactness low (cf. Sec. 2.6).

$$R_{\text{eff}} \approx R_0 \left[1 + \alpha \left(\frac{\epsilon_{\text{coup}}}{\epsilon_{\text{max}}} \right) \right] r_g, \quad (5)$$

with $r_g = GM/c^2$, fiducial $R_0 \sim 10^2$ and $\alpha \sim 50$.

2.6. Transparency (Compactness Constraint)

In brief — Transparency requires $\ell \lesssim 30$, linking power deposition to geometry and spectrum.

Transparency requires pair compactness

$$\ell = \frac{L_{\text{self}} \sigma_T}{4\pi R_{\text{eff}} m_e c^3} \lesssim 30, \quad (6)$$

which couples Eqs. (4) and (5) and motivates $R_{\text{eff}} \sim 10^2\text{--}10^3 r_g$ during bright episodes. We adopt $\ell \lesssim 30$ as a conservative transparency threshold following classic compactness arguments; the precise value depends on geometry and spectrum and can be re-tuned in data applications. See, e.g., (R. Svensson 1984; A. P. Lightman & A. A. Zdziarski 1987).

2.7. Spin and Mass Evolution

In brief — Torque balance with Ω_H enforces a -drift toward an equilibrium a_{eq} below unity.

The horizon angular frequency is

$$\Omega_H = \frac{a_* c^3}{2GM(1 + \sqrt{1 - a_*^2})}, \quad (7)$$

where $r_H = r_g(1 + \sqrt{1 - a_*^2})$ and $r_g = GM/c^2$. Evolution obeys

$$\frac{dM}{dt} = \frac{dM_{\text{acc}}}{dt} - \frac{P_{\text{ext}}}{c^2}, \quad (8)$$

$$\frac{dJ}{dt} = \frac{dJ_{\text{acc}}}{dt} - \frac{P_{\text{ext}}}{\Omega_H}, \quad (9)$$

$$\frac{da_*}{dt} = \frac{c}{GM^2} \frac{dJ}{dt} - 2a_* \frac{1}{M} \frac{dM}{dt}. \quad (10)$$

2.8. Net Luminosity

In brief — Total luminosity combines accretion and equatorial feedback, naturally yielding $L/L_{\text{Edd}} \sim 2\text{--}3$.

The total luminosity is

$$L_{\text{tot}} = L_{\text{acc}} + L_{\text{self}}, \quad L_{\text{acc}} \approx \eta_{\text{acc}} \left(\frac{dM_{\text{acc}}}{dt} \right) c^2, \quad (11)$$

which links the dynamical solution (Eqs. (8)–(10)) to observables.

Energetic sanity check (one-line).—With $M_{\text{BH}} = 10^9 M_\odot$ [$Mc^2 \simeq 1.8 \times 10^{63}$ erg] and $E_{\text{rot}} \sim 0.1 Mc^2$, a reservoir e-fold $\tau = 10^7$ yr, $\epsilon_{\text{coup}} = 0.05$, and duty $d = 0.2$ yield $L_{\text{self}} \sim (E_{\text{rot}}/\tau)(\epsilon_{\text{coup}}/d) \approx 1.4 \times 10^{47}$ erg s $^{-1} \sim 1.1 L_{\text{Edd}}$, and 2–3 L_{Edd} when combined with concurrent accretion, while $da_*/dt < 0$ prevents overspin.



Figure 3. A spin ceiling emerges from torque balance. (a) \dot{a} crosses zero where Eqs. (8)–(10) with Ω_H from Eq. (7) balance the torques. (b) The implied equilibrium spin a_{eq} increases with coupling ϵ_{coup} ; the shaded band marks a plausible range.



Figure 4. Near-threshold systems hover close to the ceiling. Time evolution of a_* from Eqs. (8)–(10) shows self-regulated drift toward and around a_{eq} .



Figure 5. Timescales and luminosities follow the coupling law. (a) Equilibration time τ_{eq} versus coupling ϵ_{coup} . (b) L/L_{Edd} versus equilibrium spin a_{eq} , with points labeled by ϵ_{coup} (cf. Eqs. (1), (2), (11)).

3. RESULTS

In brief — Model trends map directly to hooks; figures follow their defining equations to prevent misalignment.

The figures embedded in Sec. 2 visualize each theoretical ingredient immediately after the defining equations to avoid misalignment between formulae and diagnostics. Here we summarize cross-implications and observational hooks.

3.1. Observational Hooks

In brief — After screens, three hooks—MeV shoulder, lag hardening, and equator-aligned polarization—should co-occur in the bright, high-spin subset.

Why this matters. What to look for and how to falsify, in plain terms.

Recall. Activation $\epsilon_{\text{coup}}(a_*)$ and power $P_{\text{eq}} = \epsilon_{\text{coup}} \dot{M} c^2 g(\ell)$ (cf. Eqs. (2), (11)), with transparency set by compactness ℓ (Eq. (6)). These establish the trends in the plots below.

Screens (apply first). Exclude heavy absorption (Compton-thick etc.), extreme inclination, and high compactness ($\ell \gtrsim 30$).

Hooks (apply jointly under the screens).

- **Hard X/MeV shoulder (20–120 keV, obs):** model comparison favors a shoulder over a featureless baseline by ΔAICc or $\Delta\text{BIC} \geq 6$ (rest ~ 0.3 –1 MeV at $z \gtrsim 6$).
- **Lag hardening (X→UV/optical):** energy-resolved lags increase *monotonically* with photon energy within an epoch.
- **Equator-aligned X-ray polarization (2–10 keV):** EVPA \parallel equator; polarization degree increases toward high spin/high λ .

Falsification. In vetted high-spin, high- λ quasars, *failure to recover at least two hooks* after the screens above *refutes* the framework.

At a glance. How power repartitions at high λ across mechanisms.

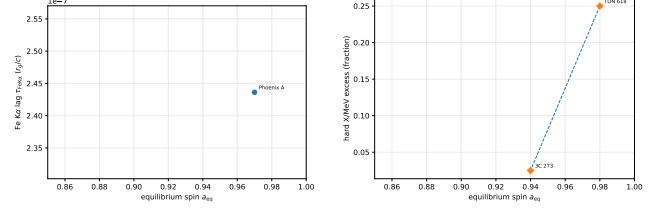


Figure 6. What each hook should look like (linked to the equations). (a) Fe K α lag (in r_g/c) versus a_{eq} . (b) Observable fraction (hard X/MeV or polarization) versus a_{eq} .

Table 1. Bottom line: the equatorial channel sustains $L/L_{\text{Edd}} > 1$ *and* imposes a spin ceiling $a_{\text{eq}} \approx a_{\text{th}}$, complementary to slim-disk (no ceiling) and BZ/MAD (polar power, $a_{\text{eq}} \sim 0.5\text{--}0.7$).

	$L/L_{\text{Edd}} > 1$	spin ceiling	channel
Slim disk	yes (advective)	no	radiation (disk)
BZ/MAD	indirect	yes ($a_{\text{eq}} \sim 0.5\text{--}0.7$)	polar Poynting (jet)
This work	yes (equatorial)	yes ($a_{\text{eq}} \approx a_{\text{th}}$)	equatorial Penrose-like

4. DISCUSSION

In brief — The equatorial branch complements polar BZ; an anti-correlated see-saw is expected across states.

These bounds align with Fig. 7–8 and are sufficient to reach $L/L_{\text{Edd}} \sim 2\text{--}3$ with rarer $5\text{--}10\times$ excursions. Slim disks allow modest super-Eddington flows but no spin ceiling. BZ/MAD explain jet power yet not the radiative dominance of radio-quiet quasars. This framework ties hyperluminous output and the spin ceiling via near-extremal, equatorial coupling. Consistent with GRFFE/GRMHD studies, an *equatorial return-current sheet forms within the ergoregion* and becomes plasmoid-unstable; detached plasmoids naturally split into branches with $E - \Omega_H L \leq 0$ (captured vs. escaping), enabling rotational-energy extraction via a Penrose-like radiative channel (R. Penrose 1969; R. Penrose 2002; S. S. Komissarov 2004; W. E. East & H. Yang 2018; Z. Pan 2018; K. Parfrey et al. 2019; A. Bransgrove et al. 2021).

Relation to Blandford–Znajek jets. BZ is polar/Poynting-dominated; our mechanism is equatorial/radiative. Hybrid states and an anti-correlated see-saw are expected; counterexamples (simultaneously strong jets and high radiative output) can occur in transitional MAD-like regimes.

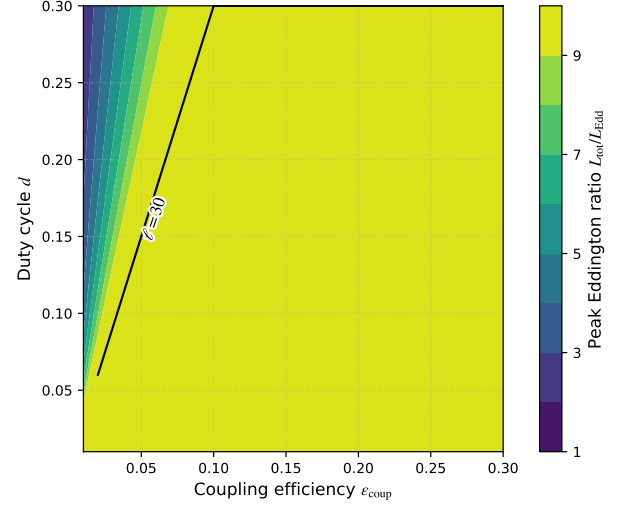


Figure 7. Transparency selects the viable high-luminosity regime (a). For $R_{\text{eff}} = 100 r_g$, the allowed region lies *outside* $\ell=30$ (black), where peak $L_{\text{tot}}/L_{\text{Edd}}$ (color) reaches 2–3 with rarer $5\text{--}10\times$ excursions.

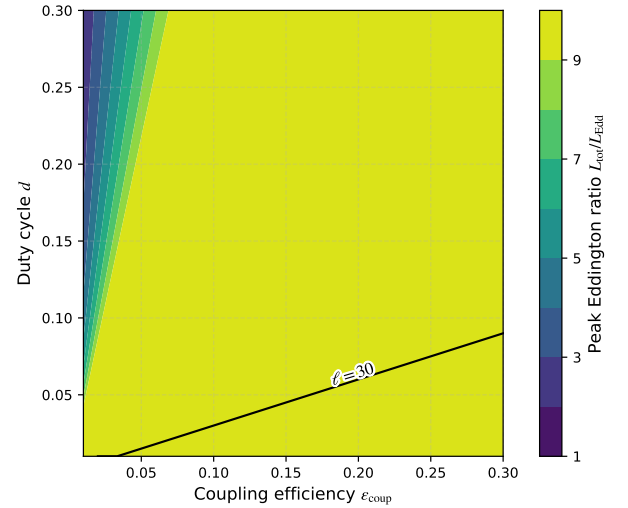


Figure 8. A larger dissipation footprint widens the transparent window (b). For $R_{\text{eff}} = 1000 r_g$, the $\ell=30$ boundary (black) shifts so that higher peaks in $L_{\text{tot}}/L_{\text{Edd}}$ remain compactness-safe.

Power partition between polar and equatorial channels.— We model the spin-extraction power as a partition between a polar Blandford–Znajek (BZ) channel and an equatorial feedback channel,

$$P_{\text{tot}} = P_{\text{BZ}} + P_{\text{eq}}, \quad (12)$$

$$P_{\text{BZ}} = f_{\text{BZ}} P_{\text{ext}}, \quad P_{\text{eq}} = f_{\text{eq}} P_{\text{ext}}, \quad (13)$$

$$f_{\text{BZ}} + f_{\text{eq}} = 1. \quad (14)$$

This partition predicts an anti-correlation between radio-jet dominance and equatorial reheating diagnostics within the high- a_* , high- λ subset, with hybrid states possible in transient MAD phases. Our claim is modest: in the high-spin, high-Eddington subset, f_{eq} is statistically non-zero and sometimes dominant; in others, f_{BZ} may prevail. Outside this subset we make no claim.

VALIDATION ROADMAP: OBSERVATIONS AND SIMULATIONS

4.1. Validation Roadmap

In brief — Polarization–spin trends, intra-epoch lag slopes, and compactness screens lead; GRMHD+RT+population studies anchor the pipeline.

Observational fronts.

- (i) **Polarization vs. spin.** Test that EVPA is equator-aligned and that the degree rises with a_*/λ ; control for jet and scattering-cone geometries; report rank-correlation p -values and effect sizes.
- (ii) **Lag hardening.** Within single epochs, verify that $X \rightarrow \text{UV}$ /optical lags increase monotonically with photon energy; mask absorption events; provide cadence/noise tests.
- (iii) **Spectral compactness screen.** Use cutoff-energy/pair proxies to flag high- ℓ cases (non-transparent) and separate them from the transparent sample used for hooks.
- (iv) **See-saw with BZ.** In jet-dominated sources, test anti-correlation between polar Poynting dominance and equatorial radiative signatures across states.

Simulation fronts.

- (i) **GRMHD near the ergoregion.** Resolve the equatorial return current sheet; quantify energy partition into positive/negative branches ($E - \Omega_H L \gtrless 0$); compare with torque-balance trends.

- (ii) **Radiative transfer with pairs.** Propagate hard X/MeV emission through compactness-limited media; map when the shoulder survives vs. is quenched (link to ℓ cut).

- (iii) **Population modeling.** Combine spin distributions with transparency and coupling priors to predict the fraction of sources passing ≥ 2 hooks.

What would falsify this framework (kill shots).—We explicitly delineate outcome patterns under which the equatorial channel is unnecessary. In the high-spin, high- λ subset (e.g., $a_* \gtrsim 0.8$, $\lambda \equiv L_{\text{bol}}/L_{\text{Edd}} \gtrsim 0.3$), any of the following, if established *as a population trend*, would falsify our claim:

1. Systematic absence of the EUV/soft-X/MeV excess (no “shoulder”) *and* systematically weak high-ionization lines (He II, N V, C IV) relative to the parent population.
2. Reverberation lags from $X \rightarrow \text{UV}$ showing no energy dependence (no inward reheating signature).
3. L_{bol} not anti-correlated (even weakly) with a_* within the bright subset (no self-regulated spin-down imprint).
4. Optical/X-ray polarization failing to favor equatorial angles or degrees when near-threshold spins are inferred.

If *two or more* items above hold simultaneously for the same high-spin, high- λ subset, we would consider $f_{\text{eq}} \rightarrow 0$ supported and this mechanism unnecessary.

5. CONCLUSION

In brief — Recovering ≥ 2 hooks under screens supports the framework; systematic absence in high-spin/high- λ would falsify it.

Self-sustained Penrose excitation near extremal Kerr SMBHs can inject rotational energy into the accretion disk, yielding sustained 2–3 \times Eddington with rarer 5–10 \times episodes while enforcing a spin ceiling.

APPENDIX

Table 2. Candidate Gallery — Representative objects; values are indicative.

Name	z	M_{BH}/M_{\odot}	L/L_{Edd}	Notes
TON 618	2.219	$\sim 6.6 \times 10^{10}$	~ 3	Extremely massive; radio-loud; literature refs. ^{<i>a</i>}
J2157-3602	4.75	$\sim 3.4 \times 10^9$	$\gtrsim 10$	Hyper-luminous; super-Eddington episode indications. ^{<i>b</i>}
J0100+2802	6.30	$\sim 1.2 \times 10^{10}$	~ 2	$z > 6$ luminous quasar. ^{<i>c</i>}
J0439+1634	6.51	$\sim 7 \times 10^9$	$\sim 2-3$	Possible lensing history. ^{<i>d</i>}

NOTE—Values are illustrative; per-object sourcing is out of scope.

^{*a*}Virial-factor dominated systematics; radio-loud bias possible.

^{*b*}Bolometric/line-width systematics $\gtrsim 0.3$ dex.

^{*c*}High- z mass methods differ (reflection vs. continuum).

^{*d*}Historical lensing debate; values assume de-lensing consensus.

CAUTIONARY NOTE.

Claims here are modular and falsifiable. Alternative mechanisms may dominate in other classes.

AUTHOR CONTRIBUTIONS

Conceptualization, modeling, analysis, visualization, and writing: J. Wakabayashi.

COMPETING INTERESTS

The author declares no competing interests.

DATA AND CODE AVAILABILITY

All figures can be regenerated from scripts in the accompanying repository; data sources and acquisition steps are documented in a README.

An archived OSF snapshot (Version 1.1) is available: <https://doi.org/10.17605/osf.io/62gzv>.

COMMUNICATION AND MEDIA

Media note: The paper and its reproducibility package are the sole authoritative sources.

ACKNOWLEDGMENTS

This work stands on decades of insight into black-hole accretion, spin, and energy extraction. I am indebted to the community that built the modern framework of quasar physics—from classical Penrose energy extraction and disk theory to spin-jet coupling and polarimetry—and to teams who made public data and tools available.

Use of large language models. Large language model assistants (Google Gemini and OpenAI ChatGPT) were used for drafting support (editing for clarity, formatting suggestions, and figure placement/LaTeX troubleshooting). No novel data, equations, or results were produced by these tools. No confidential or unpublished data were provided to them. All analysis, derivations, and conclusions are by the author, who takes full responsibility for the content; the models are not authors.

I also thank colleagues and readers who provided critical comments on early drafts. Any remaining errors are mine.

Software: `latexmk`, AASTeX701

REFERENCES

- Abramowicz, M. A., Czerny, B., Lasota, J.-P., & Szuszkiewicz, E. 1988, *The Astrophysical Journal*, 332, 646, doi: [10.1086/166683](https://doi.org/10.1086/166683)
- Blandford, R. D., & Znajek, R. L. 1977, *Monthly Notices of the Royal Astronomical Society*, 179, 433, doi: [10.1093/mnras/179.3.433](https://doi.org/10.1093/mnras/179.3.433)
- Bransgrove, A., Beloborodov, A. M., & Parfrey, K. 2021, *Physical Review Letters*, 127, 055101, doi: [10.1103/PhysRevLett.127.055101](https://doi.org/10.1103/PhysRevLett.127.055101)
- Cackett, E. M., & Zoghbi, A. 2021, *iScience*, 24, 102557, doi: [10.1016/j.isci.2021.102557](https://doi.org/10.1016/j.isci.2021.102557)
- Connor, T., Stern, D., Bañados, E., & Mazzucchelli, C. 2021, *ApJL*, 922, L24, doi: [10.3847/2041-8213/ac37b5](https://doi.org/10.3847/2041-8213/ac37b5)
- East, W. E., & Yang, H. 2018, *Physical Review D*, 98, 023008, doi: [10.1103/PhysRevD.98.023008](https://doi.org/10.1103/PhysRevD.98.023008)
- Gralla, S. E., & Jacobson, T. 2014, *Monthly Notices of the Royal Astronomical Society*, 445, 2500, doi: [10.1093/mnras/stu1690](https://doi.org/10.1093/mnras/stu1690)
- Komissarov, S. S. 2004, *Monthly Notices of the Royal Astronomical Society*, 350, 427, doi: [10.1111/j.1365-2966.2004.07672.x](https://doi.org/10.1111/j.1365-2966.2004.07672.x)
- Lai, S., Wolf, C., Onken, C. A., & Bian, F. 2023, *MNRAS*, 521, 3682, doi: [10.1093/mnras/stad651](https://doi.org/10.1093/mnras/stad651)
- Lightman, A. P., & Zdziarski, A. A. 1987, *ApJ*, 319, 643
- Pan, Z. 2018, *Physical Review D*, 98, 043023, doi: [10.1103/PhysRevD.98.043023](https://doi.org/10.1103/PhysRevD.98.043023)
- Parfrey, K., Philippov, A. A., & Cerutti, B. 2019, *Physical Review Letters*, 122, 035101, doi: [10.1103/PhysRevLett.122.035101](https://doi.org/10.1103/PhysRevLett.122.035101)
- Penrose, R. 1969, *Nuovo Cimento Rivista Serie*, 1, 252
- Penrose, R. 2002, *General Relativity and Gravitation*, 34, 1141, doi: [10.1023/A:1016578408204](https://doi.org/10.1023/A:1016578408204)
- Reynolds, C. S. 2014, *SSRv*, 183, 277, doi: [10.1007/s11214-013-0006-6](https://doi.org/10.1007/s11214-013-0006-6)
- Sun, M., et al. 2020, *arXiv e-prints*
- Svensson, R. 1984, *MNRAS*, 209, 175, doi: [10.1093/mnras/209.2.175](https://doi.org/10.1093/mnras/209.2.175)
- Tchekhovskoy, A., Narayan, R., & McKinney, J. C. 2011, *MNRAS*, 418, L79, doi: [10.1111/j.1745-3933.2011.01147.x](https://doi.org/10.1111/j.1745-3933.2011.01147.x)
- Wakabayashi, J. 2025, *Self-Sustained Penrose Excitation of Accretion Disks*, OSF Registration (Version 1.1) doi: [10.17605/osf.io/62gzv](https://doi.org/10.17605/osf.io/62gzv)
- Young, S., Axon, D., Robinson, A., Smith, J., & Hough, J. H. 2011, in *ASP Conf. Ser.*, Vol. 449, *Astronomical Polarimetry 2008: Science from Small to Large Telescopes*, 436. <https://ui.adsabs.harvard.edu/abs/2011ASPC..449..436Y/abstract>